Research Article | Vol. 31, No. 9 / 24 Apr 2023 / Optics Express 14367
Optics EXPRESS

# Single-pixel reconstructive mid-infrared micro-spectrometer

KAICHEN DONG,[1,2,3,7,†] JIACHEN LI,[2,4,†] TIANCHENG ZHANG,[4] FANGDA GU,[5] YUHANG CAI,[1,2] NIHARIKA GUPTA,[2,5] KECHAO TANG,[6] ALI JAVEY,[2,5] JIE YAO,[1,2] AND JUNQIAO WU[1,2,4,*]

[1]*Department of Materials Science and Engineering, University of California, Berkeley, California 94720, USA*
[2]*Materials Sciences Division, Lawrence Berkeley National Laboratory, Berkeley, California 94720, USA*
[3]*Tsinghua-Berkeley Shenzhen Institute, Tsinghua Shenzhen International Graduate School, Tsinghua University, Shenzhen 518055, China*
[4]*Applied Science and Technology Graduate Group, University of California, Berkeley, California 94720, USA*
[5]*Department of Electrical Engineering & Computer Sciences, University of California, Berkeley, California 94720, USA*
[6]*Key Laboratory of Microelectronic Devices and Circuits (MOE), School of Integrated Circuits, Peking University, Beijing 100871, China*
[7]*dkc22@sz.tsinghua.edu.cn*
[†]These authors contributed equally to this work
[*]*wuj@berkeley.edu*

**Abstract:** Miniaturized spectrometers in the mid-infrared (MIR) are critical in developing next-generation portable electronics for advanced sensing and analysis. The bulky gratings or detector/filter arrays in conventional micro-spectrometers set a physical limitation to their miniaturization. In this work, we demonstrate a single-pixel MIR micro-spectrometer that reconstructs the sample transmission spectrum by a spectrally dispersed light source instead of spatially grated light beams. The spectrally tunable MIR light source is realized based on the thermal emissivity engineered via the metal-insulator phase transition of vanadium dioxide ($VO_2$). We validate the performance by showing that the transmission spectrum of a magnesium fluoride ($MgF_2$) sample can be computationally reconstructed from sensor responses at varied light source temperatures. With potentially minimum footprint due to the array-free design, our work opens the possibility where compact MIR spectrometers are integrated into portable electronic systems for versatile applications.

© 2023 Optica Publishing Group under the terms of the Optica Open Access Publishing Agreement

## 1. Introduction

Optical spectroscopy is among the most widely used characterization techniques for both industrial processes and scientific research [1–4]. Conventional bench optical spectrometers offer exceptional spectral resolution in various wavelength ranges, but their bulky optical systems severely hamper further applications where reduced size and cost are vital [4,5]. Therefore, the miniaturization of optical spectrometers has become a cutting-edge research field with huge potential in the consumer market [6]. Existing strategies to realize compact optical spectrometers involve one or more of microfabricated dispersive optics [7,8] and narrowband filters [9–11], Fourier transform [12,13], microelectromechanical systems (MEMS) [14,15], and computational reconstruction [16–19]. Compared to other strategies, computationally reconstructive spectrometers mitigate the requirements on micro-optical systems (e.g., gratings and micro-mechanics) by computational techniques [4,20], and are promising in the market of consumer electronics like smartphones and portable instruments [4,21]. As such, in the past

#485934 https://doi.org/10.1364/OE.485934
Journal © 2023 Received 18 Jan 2023; revised 3 Mar 2023; accepted 3 Mar 2023; published 17 Apr 2023

Optics EXPRESS

decade, the new paradigm of reconstructive micro-spectrometers has quickly gained interests with demonstrations based on nanowires [4], van der Waals materials [1], or quantum-dots [22].

However, the computational reconstruction of spectrum requires an enough number of equations to avoid the underdetermination of problems [4]. Otherwise, additional information of the target spectrum needs to be incorporated to find the most reasonable/trustworthy solution [23], which would limit the applications. Hence, arrays of detectors or filters are essential in most reconstructive spectrometers, such as detection channels [19], structurally colored nanowires [24], photonic crystal slabs [25], multiple electrodes [2], etc. Due to their physical sizes and fabrication-limited resolution, these arrays become the obstacle to further miniaturization of micro-spectrometers.

In this work, we propose and experimentally implement a miniaturized reconstructive spectrometer without detector/filter arrays. By tailoring distinct emissivity spectra for the light source with a phase transition at different temperatures, a single-pixel MIR (8-12 μm) micro-spectrometer is demonstrated. Unlike conventional reconstructive spectrometers that requires spatially distributed arrays to acquire reconstruction equations, this work obtains the equation set by simply varying the light source temperature and thus its spectral emission, which overcomes the dimensional limitations imposed by array structures. The focus of this work is proposing a new strategy for MIR micro-spectrometers with potentially the smallest footprint, though the spectrum reconstruction accuracy and resolution of our demonstration (in its current form) need improvement.

## 2. Experiments and results

### 2.1. Micro-spectrometer and MIR light sources

Figure 1 shows the schematic of this micro-spectrometer, which consists of a MIR light source and a MIR sensor (D6T-1A-02, Omron) installed at both ends of a cylindrical chamber. The temperature-dependent MIR emission spectrum of the light source is controlled by a customized heating stage. The light source temperature is read by a temperature sensor on the heating stage. The interior surface of the chamber is highly reflective to maximize the portion of light that goes through the sample to be collected by the sensor. Moreover, the reflective chamber surface also minimizes unnecessary thermal emission from the chamber wall. During the measurement, the sample is placed in the chamber between the light source and the sensor, whose MIR transmittance will be measured.

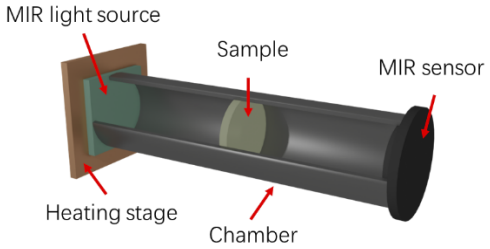


**Fig. 1.** Schematic of the single-pixel reconstructive micro-spectrometer.

The micro-spectrometer should be judiciously designed to enhance the reconstruction accuracy and minimize the influence of ill-posed inversion problem for spectrum reconstruction [4]. Here, we designed and fabricated a MIR light source showing temperature-dependent spectral emissivity based on the metal-insulator phase transition of $VO_2$ [26–28]. As shown in Fig. 2(a), lithographically patterned tungsten (W) blocks with a periodicity of 2.5 μm are embedded in a 150 nm-thick $VO_2$ film prepared by pulsed laser deposition (PLD). The width and thickness of the

Optics EXPRESS

W blocks are 1.3 µm and 50 nm, respectively. The above layers sit on top of a 200 nm-thick barium fluoride ($BaF_2$) dielectric spacer and a 130 nm-thick silver (Ag) mirror. Detailed fabrication procedures can be found in Supplement 1, Note S1. This light source (hereafter termed as a $VO_2$ metastructure) is mechanically flexible and suitable for various micro-spectrometer designs, as it can be attached to non-flat solid surfaces (Fig. 2(b)). Meanwhile, its small thickness (< 100 µm even with the supporting Scotch tape included) ensures fast thermal response and temperature uniformity. We note that all the W blocks are of the same size and periodicity, so that the W array in the $VO_2$ metastructure together forms a single-pixel photonic light source, which when partially damaged, would not lose its functionality. In contrast, conventional photonic filter arrays have multiple physical sections with different photonic structures, where each section serves as only one pixel [9,11,29,30].

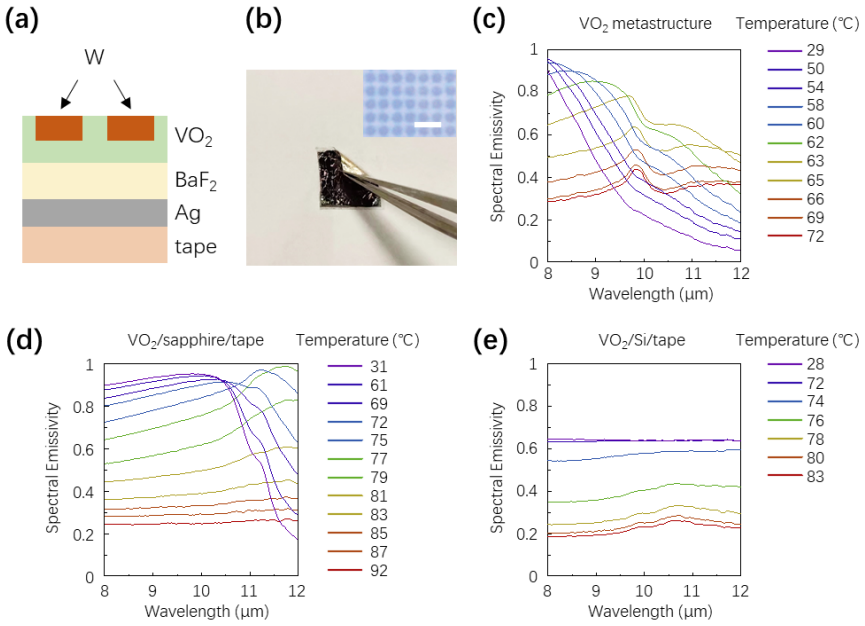


**Fig. 2. MIR light source.** (a) Schematic diagram of the cross-sectional view of the $VO_2$ metastructure (not drawn to scale). (b) Photo of the $VO_2$ metastructure on tape showing flexibility under bending. Inset: microscopic image of the metastructure pattern. Scale bar is 5 µm. (c-e) Spectral emissivity at different temperatures for the $VO_2$ metastructure (c), as well as $VO_2$ film on sapphire (d) and $VO_2$ film on Si (e) for comparison. The complete sets of data are in Supplement 1, Note S2.

The spectral reflectivity of the $VO_2$ metastructure as a function of temperature was measured by Fourier-transform infrared spectroscopy (FTIR, Nicolet iS50, Thermal Scientific) and the corresponding spectral absorptivity was calculated with a zero transparency. Note that the temperature went up monotonically during the measurements. According to Kirchhoff's law of radiation [31,32], the $VO_2$ metastructure emissivity equals its absorptivity and is shown in Fig. 2(c). $VO_2$ undergoes a rapid and reversible phase transition from the insulating (I) phase to metallic (M) phase upon heating beyond its transition temperature, accompanied by a drastic change in its MIR optical properties [27,28,33]. Due to the high-temperature $VO_2$ growth and annealing process, W diffusion from the W blocks into the $VO_2$ layer decreases its phase-transition temperature for faster spectrometer measurements [34,35]. At lower temperatures, the I-phase $VO_2$ film is a transparent dielectric to the MIR [28,34], so the whole metastructure is effectively a trilayer absorptive metamaterial whose emissivity peak is identical to its absorption peak at

Optics EXPRESS

7.5 μm (Fig. 2(c)), which results from the in-plane photonic mode at the W block array (details in Supplement 1, Note S3). On the other hand, at high temperatures the $VO_2$ layer switches to M phase with a strong reflection to the MIR [28,34], leading to much reduced thermal emission from the $VO_2$ metastructure. Detailed analysis and description of the metastructure are in Supplement 1, Note S3. Due to the polycrystalline nature of the $VO_2$ thin films, a wide intermediate range exists between its full I phase at low temperature (e.g., 29 °C) and full M phase at high temperature (e.g., 72 °C), which generates a series of nonlinearly distinct emissivity spectra with the increasing temperature, offering an enough number of equations for the post-measurement reconstruction.

To justify the effectiveness of this strategy, two other MIR light sources without the W-block micro-patterns were also tested. 200 nm-thick $VO_2$ films were pulsed laser deposited onto sapphire and silicon substrates, and then attached onto a high-emissivity tape [28,34] to eliminate MIR transmission. Similarly, their temperature-dependent emissivity spectra were also measured by FTIR (Fig. 2(e) and 2(f)). Although the emissivity spectra of all three light sources, strictly speaking, vary nonlinearly with temperature, the $VO_2$ metastructure shows the greatest variation in the line-shape of the emissivity spectra as temperature increases. Such an advantage of the $VO_2$ metastructure comes from the relatively sharp I-phase emissivity peak at 7.5 μm, and the resultant large contrast between I-phase and M-phase spectral emissivity.

### 2.2. Calibration process

Since the demonstration was carried out in the thermal MIR range, strong noise is expected due to the omnipresent thermal radiation from all micro-spectrometer components. Hence, the reconstructive system was calibrated prior to the spectroscopic measurements of samples. As shown in Fig. 3(a), the micro-spectrometer chamber consists of two parts (herein coined as "top chamber" and bottom chamber") manufactured by a 3D printer (Ultimaker 2+, Dynamism) with acrylonitrile butadiene styrene (ABS). The 3D-printing filling density is decreased to minimize the unwanted conductive heat transfer in the chamber walls [36]. High MIR reflectance was achieved by covering the interior chamber surface with aluminum foil. In the experiments, the MIR sensor was fixed in the sensor pocket of the top chamber while the light source was taped to a heater and covered by the bottom chamber.

The calibration was conducted by measuring the sensor readout as a function of light source temperature without samples (Fig. 3(b)). The room temperature is 22.5 °C and the temperature ramp rate for heating is 10 °C/min. Here, two major components of MIR light going into the sensor are considered: direct thermal emission from the light source ($P_a$); the sensor thermal emission that is reflected by the light source ($P_b$). Assuming the integrated emissivity (=absorptance) of the sensor to be 100%, the total MIR light power ($P_{total}$) that is absorbed by the sensing part [37] of the sensor can be calculated by

$$\begin{cases} P_{total}(t) = P_a(t) + P_b(t) - P_{fit}(t) \\ P_a(t) = \int_{\lambda_{min}}^{\lambda_{max}} E_{source}(\lambda, t) \times B(\lambda, t) d\lambda \\ P_b(t) = \int_{\lambda_{min}}^{\lambda_{max}} R_{source}(\lambda, t) \times P_{sensor}(\lambda, t_{sensor}) d\lambda \end{cases} \tag{1}$$

where $t$ and $t_{sensor}$ are the light source temperature and the experimental sensor readout, respectively. Note that $P_{fit}$ and $P_{sensor}$ are fitting terms. With $\lambda$ representing wavelength, the wavelength range for the integration (i.e., $[\lambda_{min}, \lambda_{max}]$) is taken from the sensor datasheet [37]. $E_{source}$ and $R_{source}$ are the emissivity and reflectivity of the light source, respectively. $B(\lambda, T) = \frac{2hc^2}{\lambda^5} \frac{1}{e^{hc/(\lambda k_B T)} - 1}$ is the black-body spectral radiance [38]. Meanwhile, $P_{total}$ in Eq. (1) is also related to $t_{sensor}$ [39,40]. Since the specific algorithm for this sensor to derive the temperature of a target object is unknown to us, here it is calculated by:

$$P_{total}(t) = \int_{\lambda_{min}}^{\lambda_{max}} B(\lambda, t_{sensor}) d\lambda. \tag{2}$$

Optics EXPRESS

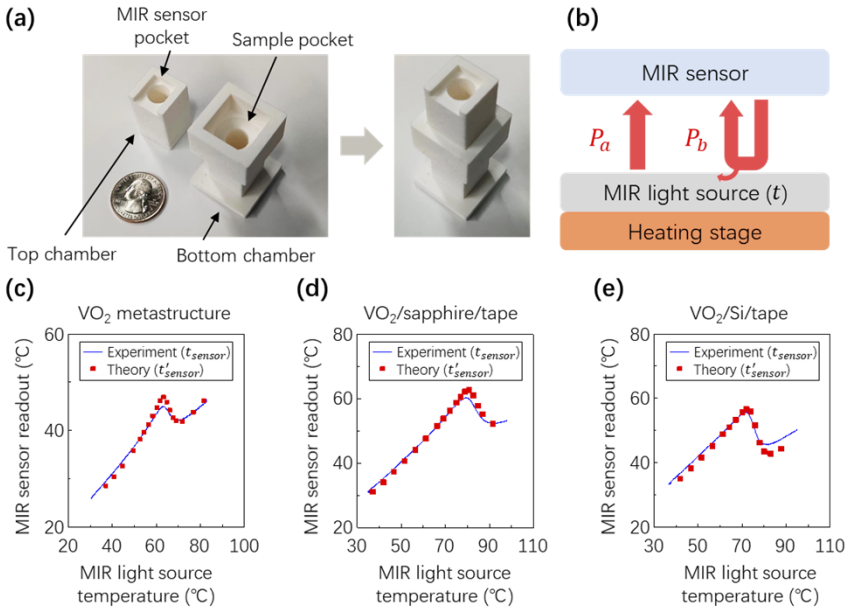


**Fig. 3. Calibration of the system.** (a) Photo of the two-part chamber. (b) Schematic of the calibration experiment. (c-e) Experimental and theoretical temperature readouts of the MIR sensor as a function of the MIR light source temperature when the light source is $VO_2$ metastructure (c), $VO_2$/sapphire/tape (d) and $VO_2$/Si/tape (e).

Note that this assumption does not affect the validity of our conclusion because the fitting parameters in Eq. (1) can accommodate the discrepancy between Eq. (2) and the actual algorithm for the sensor. Combining Eq. (1) and (2), the theoretical sensor temperature ($t'_{sensor}$) is calculated using $P_a(t)$ and $P_b(t)$. The model can thus be calibrated to minimize the discrepancies between $t'_{sensor}$ and $t_{sensor}$.

To account for the observed noise and MIR light power approximation, two fitting terms are incorporated for the calibration: an additional power-loss term ($P_{fit}$) and the thermal radiation of the sensor ($P_{sensor}$). $P_{fit}$ accounts for: (1) the MIR power absorbed by the sensor package but not by the sensing part behind the lens; (2) all noise coming from the nonuniformly heated chamber surface; (3) conductive heat loss of the hot junction in the sensor [39,40]. All these factors tend to increase with the source temperature $t$. Hence, $P_{fit}$ is approximated by the difference between $t$ and the room temperature. $P_{sensor}$ consists of the radiation from both the interior hot junction behind the sensor lens and the room-temperature exterior sensor package surfaces [37]. In Fig. 3(c) to 3(e), $t'_{sensor}$ and $t_{sensor}$ are compared with $t$ for all three light sources in Fig. 2(c) to 2(e). Details are in Supplement 1, Note S4.

### 2.3. Spectrometry test

Using the calibrated system, MIR transmission measurements were conducted. Here, we selected a 1mm-thick magnesium fluoride ($MgF_2$) window as the sample for two reasons: (1) $MgF_2$ is a widely used IR-transparent material with a low refractive index [41]; (2) the transmissivity of $MgF_2$ varies significantly in the 8-12 μm wavelength range [42], providing a remarkable feature in the transmissivity spectrum for tests. The transmissivity spectrum of the $MgF_2$ window measured by FTIR serves as the ground truth in the following tests (Fig. 4(b) and 4(c)). Also note that the MIR reflectivity of $MgF_2$ is close to zero and thus negligible in the spectrum reconstruction (Supplement 1, Note S5).

Optics EXPRESS

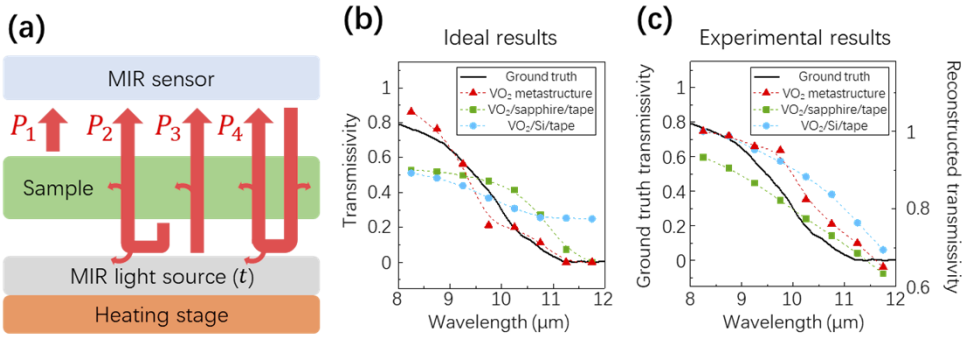


**Fig. 4. Measurements of transmissivity of a $MgF_2$ sample using the single-pixel reconstructive micro-spectrometer.** (a) Schematic of the experiment configuration. (b and c) Comparison between the ground truth and reconstructed spectra based on ideal MIR sensor readouts (b) or experimental MIR sensor readouts (c).

Spectrometry tests for the sample transmissivity were carried out and schematically illustrated in Fig. 4(a). After inserting the $MgF_2$ window into the chamber (Fig. 1), the total power received by the MIR sensor is majorly contributed by four terms: direct thermal radiation from the sample ($P_1$); thermal radiation released by the sample and reflected by the light source ($P_2$); thermal radiation that was emitted by the light source and passed through the sample ($P_3$); thermal radiation of the sensor, which was reflected by the light source and transmitted twice through the sample ($P_4$). With the calibrated system, theoretical $P_{total}$ is calculated by

$$\begin{cases} P_{total}(t) = P_1 + P_2(t) + P_3(t) + P_4(t) - P_{fit}(t) \\ P_1 = \int_{\lambda_{min}}^{\lambda_{max}} E_{sample}(\lambda) \times B(\lambda, t_{RT}) d\lambda \\ P_2(t) = \int_{\lambda_{min}}^{\lambda_{max}} T_{sample}(\lambda) \times R_{source}(\lambda, t) \times E_{sample}(\lambda) \times B(\lambda, t_{RT})\, d\lambda \\ P_3(t) = \int_{\lambda_{min}}^{\lambda_{max}} T_{sample}(\lambda) \times E_{source}(\lambda, t) \times B(\lambda, t)\, d\lambda \\ P_4(t) = \int_{\lambda_{min}}^{\lambda_{max}} T_{sample}(\lambda) \times R_{source}(\lambda, t) \times T_{sample}(\lambda) \times P_{sensor}(\lambda, t_{sensor})\, d\lambda \end{cases} \tag{3}$$

where $T_{sample}$ and $E_{sample}$ are the unknown transmissivity and emissivity spectra of the sample, respectively. Owing to the negligible reflectance of $MgF_2$ and Kirchhoff's law of radiation, here $E_{sample}$ can be replaced by $1 - T_{sample}$. $t_{RT}$ is the room temperature. Combining Eq. (2) and (3), the equation system can be obtained to reconstruct $T_{sample}$. In our spectrometer tests, $t_{sensor}$ is recorded as $t$ increases, leading to a series of experimental $t_{sensor}$ ($t^1_{sensor}$, $t^2_{sensor}$,. . . , $t^i_{sensor}$) and the corresponding $t$ ($t^1$, $t^2$,. . . , $t^i$). The equation system for spectrum reconstruction is thus described by:

$$\begin{cases} P_1 + P_2(t^1) + P_3(t^1) + P_4(t^1) - P_{fit}(t^1) = \int_{\lambda_{min}}^{\lambda_{max}} B(\lambda, t^1_{sensor})\, d\lambda \\ P_1 + P_2(t^2) + P_3(t^2) + P_4(t^2) - P_{fit}(t^2) = \int_{\lambda_{min}}^{\lambda_{max}} B(\lambda, t^2_{sensor})\, d\lambda \\ P_1 + P_2(t^i) + P_3(t^i) + P_4(t^i) - P_{fit}(t^i) = \int_{\lambda_{min}}^{\lambda_{max}} B(\lambda, t^i_{sensor})\, d\lambda \end{cases} . \tag{4}$$

The reconstruction of $T_{sample}$ based on Eq. (4) is feasible thanks to the distinct emissivity spectra ($E_{source}(\lambda, t)$) at different temperatures of the metastructure. Consequently, arrays of detectors or filters that are inevitable in convectional reconstructive spectrometers [9,11,29,30] are replaced by the single-pixel light source with in-situ tunable emission spectrum. With the

Optics EXPRESS

discretization of spectra in the calculation, the final model in matrix form is:

$$\boldsymbol{A}\boldsymbol{T}_{\boldsymbol{sample}}^{2} + \boldsymbol{B}\boldsymbol{T}_{\boldsymbol{sample}} = \boldsymbol{C} + \boldsymbol{\delta}. \tag{5}$$

In Eq. (5), vector $\boldsymbol{T}_{\boldsymbol{sample}}^{2}$ is an element-wise square of $\boldsymbol{T}_{\boldsymbol{sample}}$. Matrix $\boldsymbol{A}$ and $\boldsymbol{B}$ correspond to the quadratic and linear terms on $\boldsymbol{T}_{\boldsymbol{sample}}$ in Eq. (4). Vector $\boldsymbol{C}$ consists of all constant terms in Eq. (4). Vector $\delta$ represents the modeling error. To resolve the sample transmissivity, we minimized squared error $\delta^2$ over $\boldsymbol{T}_{\boldsymbol{sample}}$ with L2 regularization term added and physical constraints enforced. The optimization problem is given by

$$\min_{\boldsymbol{T}_{\boldsymbol{sample}},\boldsymbol{\delta}} \|\boldsymbol{\delta}\|_2^2 + \mu\|\boldsymbol{T}_{\boldsymbol{sample}}\|_2^2 \tag{6}$$

$$s.t. \quad \boldsymbol{\delta} = \boldsymbol{A}\boldsymbol{T}_{\boldsymbol{sample}}^{2} + \boldsymbol{B}\boldsymbol{T}_{\boldsymbol{sample}} - \boldsymbol{C}$$

$$\textit{physical constraints}\ .$$

Here, the L2 regularization term is $\mu||\boldsymbol{T}_{\boldsymbol{sample}}||_2^2$, which helps reduce the extent of over-fitting and $\mu \geq 0$ is the strength parameter. The physical constraints only consist of transmissivity constraints between 0 and 1 and reconstructed spectrum resolution. In practice, the optimization problem is non-convex and we solved it by optimizing the upper bound of the objective function instead. All above details are in Supplement 1, Note S7. To verify the functioning of this micro-spectrometer, we first numerically solved Eq. (5) by assuming an ideal $P_{total}$ and solving an optimization problem to minimize the objective upper bound of the problem above, and the reconstructed spectra are compared with the ground truth in Fig. 4(B) (Supplement 1, Note S6). The spectrometry measurement based on $VO_2$ metastructure successfully reconstructs the $MgF_2$ transmission spectrum with reasonable accuracy. Though the other two light sources can also partially reconstruct the spectrum, they both suffer from overwhelming noise because of the weak nonlinearity in their temperature-dependent spectral emissivity.

Next, we use experimental MIR sensor readouts for the reconstruction (Supplement 1, Note S6). As shown in Fig. 4(c), the micro-spectrometer with $VO_2$ metastructure successfully profiles the high-pass nature of $MgF_2$ as well as its cut-off frequency with a resolution of 0.5 µm. Compared to the above ideal results, the discrepancies between experimentally reconstructed spectra and the ground truth are considerable, as $P_{total}$ is underestimated in our model. The reconstruction errors can be partially fixed by considering the additional MIR power emitted from the heated $MgF_2$ window (Supplement 1, Note S8). Nevertheless, the accuracy of spectrum reconstruction with $VO_2$ metastructure is still the best among the three light sources, again proving the importance of nonlinearity in designing the light source to replace conventional detector/filter arrays.

## 3. Discussion

The use of phase-transition materials in this work enables a new paradigm for reconstructive micro-spectrometers that overcomes the challenges imposed by detector/filter arrays: (1) The footprint of array-based micro-spectrometers is no less than $N \times S$, where $N$ is the number of detectors/filters in the array while $S$ is the dimensional size of a single detector/filter (i.e., a single pixel) [9,11,29,30]. On the contrary, the theoretical minimum footprint of our single-pixel micro-spectrometer is merely $S$, because its equation system is constructed by tuning spectral emission with appropriate stimuli (e.g., temperature in this work). (2) The system models of reconstructive micro-spectrometers are normally discretized into $R$ sections to obtain numerical solutions, which is related to the resolution of the reconstructed spectrum. Failure to satisfy $R \leq N$ leads to poor numerical solutions in conventional reconstructive spectrometers [23]. Thanks to the phase-transition mechanism of $VO_2$, ideally an infinite number of equations ($N \rightarrow \infty$) can be constructed at all possible temperatures during the phase transition. Practically speaking,

Optics EXPRESS

the maximum $N$ of this single-pixel micro-spectrometer is determined by the resolution and signal-to-noise ratio of the heating stage temperature control and FTIR measurements. Therefore, the spectrum resolution of this micro-spectrometer would be improved with more advanced characterization tools. Also, compared to other tunable MIR sources, including quantum cascade lasers [43,44], the $VO_2$ metastructure design has a much larger nonlinear wavelength range for broadband spectrum reconstruction. We note that better metastructure designs can further improve the nonlinearity in temperature-dependent spectral emissivity [28,45]. Moreover, the simple structure and cheap fabrication costs show potential in some portable applications with low requirements on sensitivity and resolution.

This work has three weaknesses: (1) Though the single-pixel micro-spectrometer is promising in achieving extreme physical dimensions, it also sacrifices the response speed because of the successive nature of measurements. The shortest time for one measurement is roughly 1-2 minutes during which the $VO_2$ metastructure is heated from 58 °C to 69 °C. However, the cyclic time for continuous measurements is tens of minutes with the current design, which can be significantly improved by installing a Peltier cooler for a much higher cooling ramp rate. (2) The MIR spectrometry can only be carried out for samples with negligible reflectivity. (3) Reconstruction errors are large (Fig. 4(c)). The challenges (2) and (3) arise from the inevitable thermal radiation from all objects. For example, since the thermal radiation from the MIR sensor itself influences the result, the unknown details (temperature measurement algorithm, temperature distribution of the hot junction, etc.) of the MIR sensor need to be roughly fitted by $P_{sensor}$ and $P_{fit}$. We note that our key purpose is to demonstrate this new strategy rather than to experimentally achieve high reconstruction accuracy.

The above challenges could be addressed by the following approaches: (1) The utilization of voltage-controlled light sources (like van der Waals materials [1] and liquid crystal [46]) will significantly increase the response rate. Furthermore, replacing the stimulus from temperature to voltage can cut off unwanted thermal effects. (2) Though the current demonstration relies on the negligible reflection of $MgF_2$, future improvement could accommodate this with an alternative micro-spectrometer design for reflection measurement (Supplement 1, Note S9). (3) The spectrum reconstruction accuracy could be improved by moving to shorter wavelength ranges, calibrating all unknown technical specifications within the MIR sensor, and all improvements that help avoid the quadratic term in Eq. (5) to physically linearize the equation set [47]. With better resolution and higher reconstruction accuracy, the transmission spectrum of cellulose or thin layers of methanol may be accurately reconstructed. Moreover, a mathematical criterion with a figure of merit to judge the nonlinearity in the dependence of spectral emission on temperature of light sources for such single-pixel reconstructive micro-spectrometers will significantly benefit future researchers in this field.

## 4. Conclusion

In conclusion, aiming at the theoretically smallest footprint of MIR micro-spectrometers for portable applications, this work proposes a single-pixel reconstructive micro-spectrometer with no gratings nor detector/filter arrays. The equation system in this work is obtained by modulating the spectral emissivity of MIR light source using phase-transition materials. Based on the calibrated system, the profile of $MgF_2$ transmissivity spectrum is reproduced with its cutoff frequency identified. The comparison among three MIR sources reveals the importance of nonlinearity in the dependence of spectral emission on temperature from the tunable light sources. Indeed, the prospect of this work with the arguably smallest footprint opens the possibility of extremely miniaturized MIR spectrometers in consumer electronics such as smartphones and portable electronics.

**Funding.** National Science Foundation (ECCS-1953803); U.S. Department of Energy (DE-AC02-05-CH11231); Tsinghua Shenzhen International Graduate School (start-up funding).

Optics EXPRESS

**Acknowledgments.** This work is supported by U.S. NSF Grant No. ECCS-1953803. MIR measurements were funded by the U.S. Department of Energy, Office of Science, Office of Basic Energy Sciences, Materials Sciences and Engineering Division under contract DE-AC02-05-CH11231 (EMAT program KC1201). K.D. acknowledges the start-up funding in Tsinghua Shenzhen International Graduate School (SIGS), Tsinghua University. The authors would thank Dr. Rui Chen for help with 3D-printing. Partial measurement and fabrication were done in the U.C. Berkeley Marvell Nanolab and Biomolecular Nanotechnology Center.

**Disclosures.** The authors declare no conflicts of interest.

**Data availability.** All the data used in this study are available on request from the corresponding authors.

**Supplemental document.** See Supplement 1 for supporting content.

## References

1. H. H. Yoon, H. A. Fernandez, and F. Nigmatulin, *et al.*, "Miniaturized spectrometers with a tunable van der Waals junction," Science **378**(6617), 296–299 (2022).
2. Z. Yang, T. Albrow-Owen, and H. Cui, *et al.*, "Single-nanowire spectrometers," Science **365**(6457), 1017–1020 (2019).
3. A. Toulouse, J. Drozella, and S. Thiele, *et al.*, "3D-printed miniature spectrometer for the visible range with a 100× 100 µm2 footprint," Light: Adv. Manufact. **2**(1), 20–30 (2021).
4. Z. Yang, T. Albrow-Owen, and W. Cai, *et al.*, "Miniaturization of optical spectrometers," Science **371**(6528), eabe0722 (2021).
5. W. Deng, Z. Zheng, and J. Li, *et al.*, "Electrically tunable two-dimensional heterojunctions for miniaturized near-infrared spectrometers," Nat. Commun. **13**(1), 4627 (2022).
6. A. Li, C. Yao, and J. Xia, "Advances in cost-effective integrated spectrometers," Light: Sci. Appl. **11**(1), 174 (2022).
7. R. F. Wolffenbuttel, "State-of-the-art in integrated optical microspectrometers," IEEE Trans. Instrum. Meas. **53**(1), 197–202 (2004).
8. C. Yang, K. Shi, and P. Edwards, *et al.*, "Demonstration of a PDMS based hybrid grating and Fresnel lens (G-Fresnel) device," Opt. Express **18**(23), 23529–23534 (2010).
9. S.-W. Wang, C. Xia, and X. Chen, "Concept of a high-resolution miniature spectrometer using an integrated filter array," Opt. Lett. **32**(6), 632–634 (2007).
10. N. K. Pervez, W. Cheng, and Z. Jia, *et al.*, "Photonic crystal spectrometer," Opt. Express **18**(8), 8277–8285 (2010).
11. A. Tittl, A. Leitis, and M. Liu, *et al.*, "Imaging-based molecular barcoding with pixelated dielectric metasurfaces," Science **360**(6393), 1105–1109 (2018).
12. O. Manzardo, H. P. Herzig, and C. R. Marxer, *et al.*, "Miniaturized time-scanning Fourier transform spectrometer based on silicon technology," Opt. Lett. **24**(23), 1705–1707 (1999).
13. A. V. Velasco, P. Cheben, and P. J. Bock, *et al.*, "High-resolution Fourier-transform spectrometer chip with microphotonic silicon spiral waveguides," Opt. Lett. **38**(5), 706–708 (2013).
14. J. P. Carmoa, R. P. Rocha, and M. Bartek, *et al.*, "A review of visible-range Fabry-Perot microspectrometers in silicon for the industry," Opt. Laser Technol. **44**(7), 2312–2320 (2012).
15. P. M. Zavracky and E. Hennenberg, "Miniature Fabry Perot Spectrometers Using Micromachining Technology," Proc. WESCON **95**, 325–332 (1995).
16. T. Yang, C. Xu, and H.-P. Ho, *et al.*, "Miniature spectrometer based on diffraction in a dispersive hole array," Opt. Lett. **40**(13), 3217–3220 (2015).
17. B. Redding, S. F. Liew, and Y. Bromberg, *et al.*, "Evanescently coupled multimode spiral spectrometer," Optica **3**(9), 956–962 (2016).
18. P. Wang and R. Menon, "Computational spectrometer based on a broadband diffractive optic," Opt. Express **22**(12), 14575–14587 (2014).
19. B. Redding, S. F. Liew, and R. Sarma, *et al.*, "Compact spectrometer based on a disordered photonic chip," Nat. Photonics **7**(9), 746–751 (2013).
20. E. Huang, Q. Ma, and Z. Liu, "Etalon array reconstructive spectrometry," Sci. Rep. **7**, 1–6 (2017).
21. Z. Xuan, Z. Wang, and Q. Liu, *et al.*, "Short-Wave Infrared Chip-Spectrometer by Using Laser Direct-Writing Grayscale Lithography," Adv. Opt. Mater. **10**(19), 2200284 (2022).
22. J. Bao and M. G. Bawendi, "A colloidal quantum dot spectrometer," Nature **523**(7558), 67–70 (2015).
23. C.-C. Chang and H.-Y. Lin, "Spectrum reconstruction for on-chip spectrum sensor array using a novel blind nonuniformity correction method," IEEE Sens. J. **12**(8), 2586–2592 (2012).
24. J. Meng, J. J. Cadusch, and K. B. Crozier, "Detector-only spectrometer based on structurally colored silicon nanowires and a reconstruction algorithm," Nano Lett. **20**(1), 320–328 (2020).
25. Z. Wang, S. Yi, and A. Chen, *et al.*, "Single-shot on-chip spectral sensors based on photonic crystal slabs," Nat. Commun. **10**, 1–6 (2019).
26. D. Fu, K. Liu, and T. Tao, *et al.*, "Comprehensive study of the metal-insulator transition in pulsed laser deposited epitaxial $VO_2$ thin films," J. Appl. Phys. **113**(4), 043707 (2013).
27. K. Dong, S. Hong, and Y. Deng, *et al.*, "A Lithography-Free and Field-Programmable Photonic Metacanvas," Adv. Mater. **30**(5), 1703878 (2018).

Optics EXPRESS


28. K. Tang, K. Dong, and J. Li, *et al.*, "Temperature-adaptive radiative coating for all-season household thermal regulation," Science **374**(6574), 1504–1509 (2021).
29. J. H. Correia, G. de Graaf, and S. H. Kong, *et al.*, "Single-chip CMOS optical microspectrometer," Sens. Actuators, A **82**(1-3), 191–197 (2000).
30. Q. Hang, B. Ung, and I. Syed, *et al.*, "Photonic bandgap fiber bundle spectrometer," Appl. Opt. **49**(25), 4791–4800 (2010).
31. X. A. Zhang, S. Yu, and B. Xu, *et al.*, "Dynamic gating of infrared radiation in a textile," Science **363**(6427), 619–623 (2019).
32. J. A. Schuller, T. Taubner, and M. L. Brongersma, "Optical antenna thermal emitters," Nat. Photonics **3**(11), 658–661 (2009).
33. T. Driscoll, S. Palit, and M. M. Qazilbash, *et al.*, "Dynamic tuning of an infrared hybrid-metamaterial resonance using vanadium dioxide," Appl. Phys. Lett. **93**(2), 024101 (2008).
34. K. Tang, K. Dong, and C. J. Nicolai, *et al.*, "Millikelvin-resolved ambient thermography," Sci. Adv. **6**(50), eabd8688 (2020).
35. G. Karaoglan-Bebek, M. N. F. Hoque, and M. Holtz, *et al.*, "Continuous tuning of W-doped $VO_2$ optical properties for terahertz analog applications," Appl. Phys. Lett. **105**(20), 201902 (2014).
36. T. Sonsallaa, A. L. Moorea, and W. J. Meng, *et al.*, "3-D printer settings effects on the thermal conductivity of acrylonitrile butadiene styrene (ABS)," Polym. Test. **70**, 389–395 (2018).
37. D6T MEMS sensor datasheet. Retrieved 2022-12-23 from <https://components.omron.com/us-en/datasheet_pdf/A274-E1.pdf>
38. K. Tang, X. Wang, and K. Dong, *et al.*, "A thermal radiation modulation platform by emissivity engineering with graded metal–insulator transition," Adv. Mater. **32**(36), 1907071 (2020).
39. J. Schieferdecker, R. Quad, and E. Holzenkämpfer, *et al.*, "Infrared thermopile sensors with high sensitivity and very low temperature coefficient," Sens. Actuators, A **47**(1-3), 422–427 (1995).
40. A. Bao, C. Lei, and H. Mao, *et al.*, "Study on a high performance MEMS infrared thermopile detector," Micromachines **10**(12), 877 (2019).
41. M. J. Dodge, "Refractive properties of magnesium fluoride," Appl. Opt. **23**(12), 1980–1985 (1984).
42. T. F. Yen, Y. H. Chang, and D. L. Yu, *et al.*, "Diffusion bonding of $MgF_2$ optical ceramics," Mater. Sci. Eng., A **147**(1), 121–128 (1991).
43. M. S. Vitiello and A. Tredicucci, "Tunable Emission in THz Quantum Cascade Lasers," IEEE Trans. Terahertz Sci. Technol. **1**(1), 76–84 (2011).
44. M. Razeghi, W. Zhou, and S. Slivken, *et al.*, "Recent progress of quantum cascade laser research from 3 to 12 μm at the Center for Quantum Devices," Appl. Opt. **56**(31), H30–H44 (2017).
45. J. K. Pradhan, S. A. Ramakrishna, and B. Rajeswaran, *et al.*, "High contrast switchability of $VO_2$ based metamaterial absorbers with ITO ground plane," Opt. Express **25**(8), 9116–9121 (2017).
46. H. Coles and S. Morris, "Liquid-crystal lasers," Nat. Photonics **4**(10), 676–685 (2010).
47. F. M. Callier and C. A. Desoer, "*Linear system theory*," (Springer Science & Business, Media, 2012).